Proc. of AWS High Energy Electron Beam Welding & Materials Processing, 156, 1993.

HIGH ENERGY ELECTRON BEAM WELDING AND MATERIALS PROCESSING

V.R. Dave*, D. L. Goodman#, T. W. Eagar*, K. C. Russell*

ABSTRACT

High Energy Electron Beams (HEEBs) offer a unique heat source that may be used for a wide variety of materials processing applications. There are several important physical features that make HEEB - based materials processing so attractive, and the ones that will be considered here are : in-depth energy deposition, very high power levels, and shock generation capabilities. High energy electrons will penetrate several millimeters into most materials, and they allow for unique subsurface heat treatment and thermal processing. The total power levels attainable range from a few hundred kilowatts to well into the megawatt range, and the potential exists for very fast material melting processes, maybe as high as 1000 lbs / hr. Surface heat fluxes can be as high as 10^6 - 10^9 Watts / cm^2, and the possibility exists for deep penetration welding, but this will be critically analyzed below. Rapid energy deposition also results in large pressure rises within many materials, and there are many possible applications for shock hardening and shock processing. In this article, welding and shock processing will be analyzed in-depth, and it will be argued that welding may not be the application most-suited to current HEEB machines. Shock processing however does show significant promise, and other applications such as rapid melting and net-shape casting will be briefly mentioned as areas also deserving immediate attention.

HEEB ACCELERATORS AND HARDWARE

The main focus of this article is to examine applications of HEEB technology to the realm of materials processing, but HEEB accelerator technology will be briefly reviewed to provide a more complete background. This discussion will focus on a very narrow subclass of accelerators known as pulsed power linear induction accelerators. Pulsed power electron guns were originally developed to produce very short and very intense X-ray bursts. They are capable of producing extremely high beam currents and energies for quick bursts, and there are repeating machines that allow many pulses per second. There are many different designs for pulsed power accelerators. The one described here is based on the magnetic induction principle. As early as 1964, the magnetic induction principle was applied to linear electron accelerators by N.C. Christofilos. Figure 1 shows a schematic based on a paper by Christofilos et. al.(Ref. 1) A toroidal core is connected to a pulse forming network and an appropriate switch which when activated will energize the core. The electron beam threads the toroidal core, and therefore acts as the secondary of this pulse transformer. The beam is then accelerated by the induced electromotive force, and this process can be continued by stacking a series of these pulse transformers to achieve very high beam energies. The cores used by early workers were made of Ni-Fe tape that was wound into a toroidal core. Current manifestations of this principle use ferrite cores, and the drives to the acceleration units are nonlinear magnetic drives, such as the Mag-I type magnetic compressor developed at Lawrence Livermore National Laboratory (Refs. 2,3). There are many design

* Materials Science & Engineering Department, Massachusetts Institute of Technology, Cambridge, MA.
# Science Research Laboratory, Inc., Somerville, MA.

considerations and trade-offs that must be made in the construction of Linear Induction Accelerators (LIAs), and we will not enter into these details here. Briefly, the main considerations are : stable beam transport, emittance preservation, losses within ferromagnetic cores, uniformity of beam parameters, and overall accelerator efficiency (Refs. 4,5).

The complete LIA accelerator and materials processing system consists of an injector were the beam is generated, accelerator stages which boost the energy of the beam, extraction devices which bring the beam into a materials processing chamber or into the atmosphere, pulsed power drivers for the acceleration cells, vacuum systems that enclose the beamline and cathode, and various diagnostics and controls. The beam itself is generated by emission from a cathode, and is shaped, focused and accelerated by creating an anode - cathode gap. For good beam quality under repetitive operating conditions, thermionic dispenser cathodes are used. These cathodes typically consist of a tungsten matrix with other additives and surface coatings to enhance the emission properties. The anode is typically an annular structure that will allow the beam to exit into a transport region, where it is magnetically focused. The cathode and anode form a vacuum diode, and the I-V characteristic for such a diode, assuming space charge limited current, is given by the Child-Langmuir Law. For a diode of spherical geometry, this expression was calculated by Langmuir and Blodget (Ref. 6) :

$$\frac{I}{V^{3/2}} = \frac{4\varepsilon_0}{9}\sqrt{2e/m}\,\frac{4\pi}{\alpha^2} \qquad (1)$$

Where I is the current, V is the voltage across the diode, e and m are electron charge and mass respectively, and α is a constant related to the geometry of the gun.

The electron beam must be transported and focused to the final target after being generated at the cathode and accelerated by the drive stages. This may be accomplished by magnetic and electrostatic focusing. The trajectory of the electrons as they move through the transport region may be described by the basic equation of motion for a charged, relativistic particle moving through electric and magnetic fields (Ref. 7) :

$$\frac{d}{dt}\left\{\frac{m\vec{v}}{\left[1-\left(v/c\right)^2\right]^{1/2}} + e\vec{A}\right\} = -\nabla\left(e\Phi - e\vec{v}\bullet\vec{A}\right) \qquad (2)$$

Where $\vec{v}$ is the particle velocity, $\vec{A}$ is the vector potential of magnetic field, Φ is the potential of electric field, and m and e are the electron mass and charge. This expression is for single particles, and the effect of many particles interacting may be taken into account by calculating the self fields of the beam produced by space charge and beam current. To solve the full transport problem including the electron gun and beam optics system for realistic geometries is possible by a numerical approach, and EGUN is one such electron optics program. (Ref. 8). Such simulation is very important in the design of beam transport and focusing systems.

HEEB WELDING

In this section, HEEB-based deep penetration welding will be considered in detail. First, a background and overview of fusion welding processes will be given, and several concepts will be developed that will allow a critical analysis of any HEEB-based process. It will be shown that a HEEB-based process does not necessarily represent an improvement over conventional low energy electron beam welding units. This will be shown by considering the following factors : total power delivered by a HEEB process, very fast beam / material interaction times and therefore difficult control issues, HEEB pulsed power parameters that could cause material damage and expansion of fusion zone, difficulty of attaining very small spot sizes with very high current, high voltage beams, radiation problems, and cost and utilization factor considerations.

BACKGROUND ON FUSION WELDING

In fusion welding, intimate interfacial contact is achieved by interposing a liquid of substantially similar composition as the base metal. The surface contamination, if soluble, is dissolved in the liquid and, if insoluble, will float away from the liquid solid interface.

One distinguishing feature of all fusion welding processes is the intensity of the heat source used to melt the liquid. Virtually every concentrated heat source has been applied to welding from time to time : however, many of the characteristics of each heat source are determined by the intensity of the source. for example, if one considers a planar heat source diffusing into a very thick slab, the surface temperature will be a function of both the surface power density and the time. Figure 2 shows how this temperature will vary on steel with power densities ranging from 400 watts per square centimeter to 8,000 watts per square centimeter. At 400 watts / cm^2, it takes two minutes to melt the surface. If the 400 watt / cm^2 heat source were a point on the flat surface, the heat flow would be divergent and it might not even be possible to melt steel; the solid metal might be able to conduct away the heat as fast as it is being introduced. Generally, it is found that heat source power densities of approximately 1000 watts / cm^2 are necessary to melt most metals.

At the other end of the power density spectrum, it is found that heat intensities of 10^6 or 10^7 watts / cm^2 will cause vaporization of most metals within a few microseconds. Above these power densities, all of the solid interacting with the heat source is vaporized

and no fusion welding can occur. Thus it is seen that the heat sources for all fusion welding processes lie between approximately 10^3 and 10^6 watts / sq. cm on the power density spectrum. This spectrum is shown in Figure 3 with the locations of several common joining processes.

Inspection of Figure 2 shows that the power density is inversely related to the interaction time of the heat source on the material. Since this is a transient heat conduction problem, one can expect the heat to diffuse into the steel to a depth which increases as the square root of time, i.e. from the Einstein equation :

$$\delta X \propto \sqrt{\alpha t} \tag{3}$$

For planar heat sources on a steel surface as represented by Figure 2, the time in seconds to produce melting on the surface, t_m, is given by :

$$t_m = \frac{2.5 \times 10^7}{(H.I.)^2} \tag{4}$$

where H.I. is the heat intensity in watts / cm^2. If we consider the time to melting to be a characteristic interaction time, t_i, we can generate the graph shown in Figure 4. Heat sources on the order of 10^3 watts / cm^2, such as oxyacetylene flames or electroslag welding, require interaction times of 25 seconds with steel while lasers and electron beams at 10^6 watts / cm^2 need interaction times on the order of only 25 microseconds. If we divide this interaction time into the heat source diameter, D_h, we obtain a maximum travel speed, Vmax, for the welding process, as shown in Figure 5. We can approximately replace the units of watts/cm^2 of a process with the dollar cost of the capital equipment without changing the number on the axis. For example, the cost of flame welding equipment is about $1,000.00, whereas a fully automated laser or electron beam system may cost one million dollars (cf. Figure 3).

For constant total power, a decrease in the spot size will produce a squared increase in the heat intensity. This is one of the reasons why the spot size decreases with increasing heat intensity as shown in Figure 5. It is generally easier to make the spot smaller that to increase the power rating of the equipment. In addition, we generally wish to melt only a small volume of material. If the spot size were kept constant and the input power were squared in order to obtain higher densities, the volume of fused metal would increase dramatically, with no beneficial effect. However, this decreasing spot size, coupled with a decreased interaction time at higher power densities, compounds the problem of controlling the higher heat intensity process. A shorter interaction time means that the sensors and controllers for automation must operate at higher frequencies. The smaller spot size means that the positioning of the heat source must be even more precise. This positioning accuracy must be on the order of the heat source diameter. D_h, while the control frequency must be greater that the travel velocity divided by the diameter of the heat source. For processes operating near the maximum travel velocity, this is the inverse of the process interaction time, t_i (see Figure 4).

Thus we see that not only must the high heat intensity processes be automated due to an inherently high travel speed, but the fixturing requirements become greater and the control systems and sensors must have ever higher frequency response. Both of these factors lead to increased costs of high heat intensity processes, which is one reason that

laser and electron beam welding, which are very productive, have not found wider use.

Another important welding process parameter that is related to the power density of the heat source is the width of the heat affected zone. This is the zone adjacent to the weld metal, which is not melted but structurally changed due to the heat of welding. Using the Einstein equation we can estimate a heat affected zone width from the process interaction time and thermal diffusivity of the material. This shown in Figure 6 with one slight modification. Above 10^4 W / cm^2 the heat affected zone width becomes roughly constant. This is due to the fact that the HAZ grows during the heating stage at power densities below 10^4 W/cm^2 but it grows during the cooling cycle at higher power densities. Thus at low power densities, the HAZ width is controlled by the interaction time, while at high power densities it is independent of the heat source interaction time. In this latter case, the HAZ width grows during the cooling cycle as the heat of fusion is removed from the weld metal. In such a case the HAZ width is proportional to the fusion zone width.

The change of slope in Figure 6 also represents the heat intensity at which the heat utilization efficiency of the process changes. At high heat intensities, nearly all of the heat is used to melt the material and little is wasted in preheating the surroundings. As the heat intensity decreases, this efficiency is reduced. For arc welding, as little as half of the heat generated may enter the plate and only 40 percent of this heat is used to fuse the metal. For oxyacetylene welding it mat be 10 percent or less.

Finally, the heat intensity also controls the depth to width ratio of the molten pool. This can vary from 0.1 in low heat intensity processes to more than 10 in high heat intensity processes.

Thus it is seen that all fusion welding processes can be characterized generally by the heat source intensity. The properties of any new heat source can be estimated readily from the preceding graphs. The HEEB regime is one of extremely high heat source intensity, and it is clear from the preceding discussion that a HEEB heat source may be too intense. Vaporization may be a significant problem, and the pulsed power parameters of a pulsed accelerator may cause significant material damage in the form of shocks, ablation, spallation, etc. The heat input can be reduced by reducing the beam current, and this may be a possible solution in adapting the HEEB process for welding. It is useful to look more closely at conventional electron beam and laser processes as a comparison.

LASERS AND CONVENTIONAL ELECTRON BEAM WELDING PROCESSES

Laser and electron beams produce the highest heat source intensities used in welding. Although intensities of 10^9 W/cm^2 are possible, only levels of 10^6 or 10^7 are useful for welding. Above this level, vaporization of the metal is so intense that holes are drilled rather that welds being formed. In preliminary SRL / MIT experiments, this was in fact observed.

In these processes, metal vaporization begins in less than 100 microseconds, and the rapidly escaping gases produce a reaction pressure which pushes the molten metal aside, drilling a cavity in the base plate. The depth of the hole can be 50 times its width, but for practical welding conditions the depth rarely exceeds ten times the weld width. This deep narrow weld produces less thermal damage to the surrounding metal and reduces distortion as compared with other fusion welding processes. The rapid melting and high travel speeds at these high heat intensities reduce heat loss to the surroundings, with resultant melting efficiencies of 90 percent or more. Nonetheless, the narrow weld zone and high travel speed make seam tracking difficult. Misalignments or joint separation variations of 0.5 millimeter can produce defective joints ; hence preparation and fixturing of parts prior to welding is much more critical than with lower heat intensity processes. It should be noted that these same problems of controllability will persist with HEEB welding, and they may be much more severe.

The high productivity of these processes is generally only an advantage in very high volume production. The much greater capital equipment costs as compared with arc welding require that the facilities be used on a high duty cycle to achieve economy. This requires a very large volume of similar parts in order to fully utilize even small laser or electron beam machines. With HEEB machines, this could also be a consideration if the unit is fully dedicated for welding applications, although the same HEEB unit could be used for welding and materials processing with minimal modifications.

It should be recognized that there are important differences between the laser and electron beam processes and hence they cannot always be used interchangeably. Heating in an electron beam involves moderate energy electrons striking the metal, whereas laser heat is generated by an extremely large number of photons. The electrons have sufficient energy to penetrate a fraction of a millimeter beneath the surface; hence the greatest heating is subsurface; whereas laser heat is all produced on the surface of a metal. For HEEB, the penetration depth becomes significantly higher, and the heat source really becomes a volumetric heat source. This phenomenon has already been exploited using moderate energy electron beams to harden steel camshaft surfaces. Applications of HEEB for surface treatments will be discussed later in this article. In depth hardening can produce compressive stresses on the surface of the part, which are favorable as far as mechanical properties are concerned. Laser heat treatment will leave tensile surface residual stresses, making the parts prone to develop fatigue cracks in service.

The workpiece in electron beam welding must be an electrical conductor for the moderate energy beams, whereas lasers can heat insulators with equal or greater effectiveness as compared with metals. Of course with the HEEB, the electrons will now have a significant range in insulating materials as well, but charge accumulation could destroy the sample unless suitable precautions are taken.

The electron beam generally requires a vacuum for consistent results, although atmospheric electron beam machines have seen limited use. HEEB machines will hopefully extend the regime of atmospheric electron beam welding, but there are many technical issues which need to be resolved in practice, such as beam stability and transport, choice of working atmosphere (air or inert gas), and smallest achievable spot size. The laser can be more easily operated in atmospheric conditions, although helium shielding of the workpiece suppresses the formation of ionized gases above the surface of the metal. Such surface plasmas must be removed by horizontal gas flows or they will interfere with the coupling of the laser beam to the workpiece.

Electron beams are easily distorted by magnetic fields. In some cases thermoelectric currents are produced during electron beam welding of dissimilar materials. If the materials are very thick, the currents will produce magnetic fields which will distort the beam, causing it to deviate from the weld seam. Lasers, on the other hand, are not affected by stray magnetic fields.

One of the most significant problems with electron beams id that they produce X-rays. Low voltage machines of less than 30 kV produce soft X-rays which are relatively easy to shield, while moderate voltage machines of 100 kV or more require elaborate shielding. HEEB machines produce hard and potentially lethal X-rays, and shielding requirements will increase dramatically for such systems. Laser radiation is relatively easy to shield, although the beam is invisible and hence the equipment requires many safety interlocks. The laser radiation is also easily reflected by metal surfaces; hence most work must be performed inside protective enclosures.

The current of conventional electron beam welders is generally limited to 0.5 A due to beam spreading considerations. Although photons will not interact with each other, a laser beam itself can contain hot spots and cold spots due to the wave like constructive and destructive interference of the light. The beam quality of a laser is determined by the "mode" of these spots. A gaussian mode beam is the best for welding but is generally not available with laser powers above approximately 2 kW. With HEEB machines applied to atmospheric welding, the main performance limitations are imposed by Nordsieck radial expansion and the onset of the "resistive hose" instability (Refs. 9,10).

In summary, the laser and electron beam processes have many similarities and many differences. They provide some unique advantages such as low distortion and extremely rapid processing; however. they can be extremely costly except in high volume applications.

As far as HEEB process welding is concerned, there are several problems that have been listed above. Firstly, the very high heat intensity will cause significant vaporization, and drilling instead of welding may occur. The pulsed power parameters in rep-rated accelerators can cause significant material damage through shocks, spallation, and ablation. Ablation pressure may cause material blowoff and forcibly expand the size of the fusion zone Also, as in the case of conventional electron beam welders, the size of the heat affected zone will depend on the size of the fusion zone. For very high energy, high current beams, spot sizes could be much larger than what is found in conventional electron beams, and thus it is not at all obvious that HEEB systems will result in smaller heat affected zones within welded components. The high heat inputs may very well superheat the weldpiece, resulting in much larger weld pools, longer cooling times, and larger heat affected zones. These factors together with the radiation safety considerations, beam spot size limitations, and potentially low utilization factors of dedicated machines lead to the conclusion that HEEB-based welding is not a process that best utilizes the advantages of HEEB technology.

SHOCK HARDENING

As mentioned in the previous sections, a rapid deposition of radiation leads to very large temperature and pressure rises within the material. Figure 7 shows a typical energy deposition profile in Aluminum produced by a beam with a maximum energy of .4 MeV, and some energy spread about this value. For nearly instantaneous pulses, the pressure generated by irradiation has the same shape as the energy deposition profile. Also, the instantaneous temperature profile will have the same shape. The pressure and temperature profiles will then spread out and result in pressure wave propagation and overall sample heating respectively. Pressure values may be calculated by assuming that the material is very rapidly heated, and that the rise in pressure is related to the increase in internal energy of the irradiated region only. This may be expressed as :

$$\delta P = \left(\frac{\partial P}{\partial E}\right)_{V_o} \bullet \delta E \qquad (5)$$

The coefficient in parentheses is known as the Grüneisen coefficient, and is well characterized and tabulated in the literature (Ref. 11). It is possible to verify the "instantaneous" nature of these profiles by considering the possible smear in the profiles over the timeperiod of the pulse length. In the case shown, the pulse length is 50 ns, and we may find the characteristic distance for heat diffusion by assuming the material to be semi-infinite over this time period:

$$\delta X \propto \sqrt{\alpha t} \qquad (6)$$

α is .8 cm^2 / s for aluminum, and t = 50 nanoseconds. The characteristic diffusion length will only be a few microns, so we can see that the temperature profile will remain essentially constant over the time scale of 50 ns. With regards to the pressure profile, it has been observed that shock wave velocities in many materials are on the order of 10^3 m/s, and over 50 ns, the shock would only travel a few microns. So it is safe to assume that over the pulse lengths of interest, the pressure distribution also remains approximately fixed.

Figure 8 shows a typical shock-relief cycle for a compression shock generated by 1-D strain loading. This type of loading assumes that a portion of the free surface is suddenly indented. The cycle ends at point D, and it is seen that there is a permanent plastic strain associated with the passage of the shock. This permanent strain may not result in large geometric distortion, but it will produce a substantial hardening effect. In the paragraphs below, this effect is studied in much more detail to bring out its essential physical characteristics.

DISLOCATIONS AND PLASTIC DEFORMATION

In most metals over a wide range of temperatures, dislocations are the primary agents of plastic deformation. Although the net plastic strain is small, a large number of dislocations moving very fast and interacting with each other and other objects within the

crystal can result in substantial hardening. It is useful to examine more closely the mechanisms by which dislocations interact with objects in the material, and how these interactions produce hardening. Also, the effect of the large strain rates and dislocation densities that accompany shocks in metals will be considered.

Dislocations come in two flavors : edge and screw. These two are shown in Figures 9 and 10. Real dislocations in crystals are combinations of screw and edge components. There are many possible dislocation interactions, and some of these include interactions with precipitates, dispersed oxide particles, inclusions, grain boundaries, and of course with other dislocations. Each mechanism produces its own contribution to the flow stress of the material, and the study of their combined effect on the mechanical properties of the material is known as the study of work hardening. Several sub-problems within this larger problem will be examined, and their importance in shock hardening will become clear.

Before developing detailed models for the various dislocation interactions, some points in dislocation mechanics need to be invoked. The strength of a dislocation is measured by the magnitude of its Burger's Vector. The method by which the Burger's Vector may be evaluated is shown in Figure 11. Here an edge dislocation is shown with a circuit, the Burger's Circuit, drawn around it. The edge dislocation has an extra half plane to one side of it, and when an excursion is made fully around it, an extra step appears at the top portion. This extra displacement is the Burger's Vector.

Dislocations locally distort the geometry of the crystal, and as a result they have associated stress and strain fields around them. As it turns out, elasticity theory may be used to describe these fields to within a very small radius of the core of the dislocation, which represents a mathematical singular point in small strain elasticity theory. If we cut out this region from the analysis, we may find the strain energy associated with an edge a screw dislocation, and these are given by

Edge Dislocation : $$E_{edge} = \frac{Gb^2}{4\pi(1-\nu)} \bullet \ln\left(r^*\right) \tag{7}$$

Screw Dislocation : $$E_{screw} = \frac{Gb^2}{4\pi} \bullet \ln\left(r^*\right) \tag{8}$$

Where G and ν are elastic constants, $r^* = r / r_o$, and r_o is the dislocation core radius.

It is also useful to assign a line tension to a dislocation, and using this concept it is possible to find the stress needed to bend a dislocation out to a given radius. This calculation is straightforward, and is shown in Figure 12. The essential result is that the stress needed to bow a dislocation to a radius R is given by

$$\tau_0 = \frac{\alpha G b}{r} \tag{9}$$

Where α is a constant, G is an elastic constant, b is the magnitude of the Burger's Vector, and r is the radius of curvature. This result will be frequently used to study the interactions of dislocations with obstacles within the material.

Dislocations will by virtue of their associated stress fields exert forces on each other, and these may be calculated. Without entering into the details, it is found that for both types of dislocations, the forces go as 1 / r, where r is the inter-dislocation spacing. As far as the direction of these forces is concerned, screw dislocations of like sign repel, and opposite signs attract. For edge dislocations the picture is a little more complicated, but the essential result is that for edge dislocations of the same sign, they are stable when stacked on top of each other, and unstable when placed side-by-side.

We now focus attention on two other concepts needed to more fully understand dislocation interactions : dislocation sources and stacking faults. As dislocations move through the crystal and interact with other objects, many of them become "stuck" are no longer mobile. If imposed loading conditions are to be maintained, there must be a means of generating more mobile dislocations within the material, and these will replace the previously mobile dislocations which have been "stored" in various configurations. The prototypical dislocation source is the Frank-Read source, and this is shown in Figure 13. The source consists of a dislocation segment trapped between two particles and bowed out under the influence of an applied stress. If the stress reaches some critical value, the configuration of the loop will spontaneously grow out and bend back on itself, recreating the original segment and generating an outward-propagating dislocation loop.

In addition to such sources, there may be significant homogeneous nucleation of dislocation segments associated with the passage of a shock wave. Homogeneous nucleation occurs when dislocations appear in previously defect-free portions of the crystal, and Cottrell has estimated the stresses needed for this to happen (Ref. 12). The essential result is that stresses as large as G / 30 are needed to spontaneously nucleate dislocations. Typical values of G for most metals are in the range 10^6 - 10^7 psi. This means that stresses as high as 10^5 - 10^6 psi are needed. These stress magnitudes are attainable with even modest energy HEEB systems. We would therefore expect that homogeneous dislocation nucleation could play a significant role in dislocation generation associated with the passage of a shock wave.

The stacking fault is a planar defect, as are grain boundaries. These faults represent a disruption in the stacking sequence of the material, and Figure 14 shows two possible stacking faults. Stacking faults are related to dislocation mobility through the existence of partial dislocations. Partial dislocations arise when a larger dislocation splits up into two smaller ones, where the size is measured by the Burger's Vector. The smaller ones have a lower combined strain energy than the original dislocation, and there is a net energy savings. The partials are called partials because the magnitude of their Burger's Vectors may not be equal to a full lattice spacing, and thus they disrupt the stacking sequence of the material as they move. The end result is that two partials of like sign trying to get away from one another will leave a region of stacking fault between them. It takes energy to create a stacking fault however, and the balance between the stacking fault energy and strain energy of the pair of partial dislocations will determine a unique partial dislocation spacing. If the stacking fault energy is high, then the partials will stay close together, and if it is low, then they will spread out over many lattice spacings. The overall configuration of the two partials and the intermediate region of stacking fault is known as an extended dislocation. This concept is illustrated in Figure 15.

Dislocations can move from one glide plane to another, and this is known as cross slip. Where cross slip is widespread, the dislocations form complex three-dimensional tangles and bunches. If a dislocation is widely extended, it cannot easily cross-slip. Thus materials that have a high stacking fault energy and therefore small extended dislocations will be more likely to exhibit cross slip. This is a very important observation in the interpretation of dislocation structures, and some observations from experiments done using conventional shock loading techniques will be discussed below.

Hardening results from the interaction of dislocations with obstacles. These obstacles may be other dislocations themselves, and this is the first type of hardening considered. In materials in which cross slip can easily occur, dislocations will form intricate networks called cells. These consist of regions that are largely dislocation-free bounded by cell walls of high dislocation density. This is frequently observed if many FCC metals, including aluminum. Dislocations accumulate and are "stored" in such cell walls, which then act as obstacles to mobile dislocations. Dislocations may in fact have to "force" their way through the walls, and the resulting relationship between the stress needed to do this and the dislocation density was suggested first by Taylor (Ref. 13) and later analyzed in great detail by Kuhlmann-Wilsdorf (Ref. 14) :

$$\sigma \propto \sqrt{\Lambda} \tag{10}$$

Where σ is the stress and Λ is the dislocation density, measured in cm / cm^3.

If dislocations interact with precipitates, dispersed oxide particles, or inclusions, the expression for the stress needed for a dislocation to overcome an obstacle array is given by the expression :

$$\sigma \propto \frac{Gb}{l} \tag{11}$$

Where G is the shear modulus, b is the magnitude of the Burger's Vector, and l is the spacing of the obstacles. This is essentially identical to Equation 9 , and the analysis of the problem is shown in Figure 16. This equation shows the importance of closely spaced obstacles to create effective hardening via this mechanism.

Dislocations can also interact with grain boundaries, and this interaction is quantitatively described by the celebrated Hall-Petch relation :

$$\sigma = \sigma_0 + \frac{K_0}{\sqrt{\Delta}} \tag{12}$$

Where Δ is the grain diameter, σ is the applied stress, and the other terms are constants. This relationship can be derived by considering the distribution of dislocations over a limited slip plane enclosed by the boundaries of the grain. This pile-up of dislocations produces a stress concentration, and this stress has a maximum value equal to the number of dislocations times the applied external stress. Eventually this stress gets so large that dislocation sources are activated in the adjacent grain, and thus the grain boundary is effectively overcome, allowing plastic flow to proceed from grain to grain.

The hardening mechanisms outlined above together with the greatly increased dislocation density resulting from shock propagation constitute the physical basis for shock hardening. All these hardening mechanisms assume that dislocation glide is the dominant mechanism of dislocation motion in the material. In BCC metals at low temperatures, there is another important deformation mechanism known as twinning. Twinning is the occurrence of a homogeneous shear along a twinning front, which will propagate the shear throughout some region in the crystal. This process is shown schematically in Figure 17. After the front of twinning dislocations passes through the material as shown in Figure 17, a "mirror image" in terms of stacking sequence is created about a plane known as the composition plane. Twinning is important in interpreting the deformation structures of BCC materials, and it will be observed under shock loading conditions as well.

All the basic mechanisms governing dislocation movement, creation, interaction, and material hardening have been presented above. The concept of homogeneous nucleation of dislocations associated with a shock was also discussed. It is useful at this point to look at the results from previous experiments on shock loading using conventional shock loading techniques, as this will give some indication of what to expect via the HEEB process.

RESULTS FROM CONVENTIONAL SHOCK LOADING EXPERIMENTS

The table below is based on an article by W. C. Leslie (Ref. 15) presented at an AIME conference, "Metallurgical Effects at High Strain Rates" held at Albuquerque, NM in 1973. . This article is highly recommended to the interested reader as a very good overview of many experiments that have characterized the microstructure of shock-loaded metals.

MATERIAL	OBSERVED EFFECT OF SHOCK LOADING
pure copper polycrystalline	Hardness, dislocation density, stored deformation energy, yield stress, and ultimate tensile strength increase with increasing shock pressure, and then reach a maximum. Cellular dislocation structure.
pure nickel polycrystalline	Very similar to copper. At pressures above 1000 kbar, no cellular structure observed, but dislocation density very high.

pure copper single crystal	Formation of twins seen when shocks travel in [001] direction; first ever experimental observation of twinning shear in FCC metal
Aluminum	No dislocation cell structure formed up to pressures of 150 kbar, although one is expected. Structure observed was composed of randomly distributed, heavily jogged dislocations, high point defect concentration, and many dislocation loops.
FCC alloys	As stacking fault energy goes down due to alloying addition, cellular structure gives way to planar dislocation arrays, stacking faults, and twins.
Austenitic stainless steels types 302, 304, 316, & A286	Arrays of dislocations, stacking faults and twins were predominantly observed. One point of dispute : observation of α martensite in type 302 and 304. **Also, it has been recognized already that the high density of defects generated in austenite by shock loading will act as nucleation sites for precipitation of carbides and intermetallic compounds. This is especially intriguing in light of the possibility of HEEB-based combined mechanical / thermal treatments, in which the shock loading is the "pretreatment."**
Austenitic Hadfield Manganese Steel	One of the few commercial applications in use of shock loading. Mechanism of high hardening rate may be interaction between dislocations and the Mn-C complexes in solid solution in the austenite
pure iron	At pressures under 130 kbar, uniform dislocation distributions accompanied by twins. Twinning can be suppressed by pre-existing dislocation structure.
ferritic steels	Steels containing free ferrite are more susceptible to hardening. Embrittlement is also observed, and this mitigates good effects of shock hardening

The table above provides an initial guideline as to what to expect from HEEB-based shock hardening. There is also the possibility of phase transformations, and shock-induced graphite - diamond transformations have been reported using conventional shock

loading techniques (Ref. 16). A HEEB-based system offers many potential advantages over conventional shock loading since it eliminates the need for explosives and complicated flyer-plate arrangements. Also, HEEB systems can be pulsed, delivering many shocks per second while still avoiding sample overheating. The areas that can be covered are very large if the beam is de-focused, and irregularly shaped objects can also be easily processed.

HEEB POWDER PROCESSING AND NET SHAPE CASTING

As we have already seen, HEEB systems can generate strong shocks within materials, and they can also provide large heat inputs. Both these features can be effectively used for powder processing, and dynamic consolidation is a very promising application, especially for amorphous materials. Net shape casting is a process that will become very practical with the high heat intensities available from HEEBs. Metal melting rates as high as 250 - 1000 lbs. / hr are possible, and parts can be built up layer by layer, allowing for graded alloy manufacture. Turbine disks are a good first application of such a net shape casting system, and their composition can be continuously varied to produce unique components that are extremely difficult if not impossible to produce by any other route.

Metallic glasses form when liquid metal is so rapidly cooled that crystallization is kinetically inhibited. The cooling rates needed to achieve this structure are on the order of 10^6 degrees per second. Such high cooling rates have placed severe heat transfer limitations on the geometry of glassy components, and the most common forms are powders and ribbons. Making thick amorphous materials by casting is impossible due to heat transfer limitations.

Powder metallurgy offers a possible route to manufacturing bulk amorphous parts, but again heat transfer is a critical factor. If one starts with amorphous powders, any subsequent processing must not heat the material beyond its recrystallization transition temperature. Unfortunately, this temperature is so low for most metallic glasses that sintering the powders is not possible without recrystallizing them Shock processing offers a solution to this dilemma by creating a traveling zone of high pressure and temperature : the shock front. If the shock loading parameters are correctly chosen, then only the surface of the powders melts, and the powders themselves act as quenches to remove excess heat from the molten regions. This can happen very fast due to the small particle sizes involved, and the end result is that the powders stick together while remaining amorphous. This has been experimentally verified by many researchers using conventional shock loading techniques (Refs. 17,18).

HEEB. offers several distinct advantages over other shock loading processes, and these can be used to create unique bulk amorphous components. The beam can be focused or defocused to cover a wide range of areas with minimal effort. There is no limitation to

planar geometries, and with suitably clever mold design, complex three-dimensional forms could be created. Shock processing of powders could be used to dynamically sinter crystalline powders as well, and metal systems that are otherwise immiscible could be created via this route. Discontinuously reinforced composites from powders could be easily manufactured, and the high rep rates mean very high possible production speeds.

Net shape casting of turbine disks is an application that could have immediate economic benefits. The high melting rates mean very fast processing times, and if material is added in powder form, the disk could be built up layer by layer. This process can then become a very practical means for generating near net shape, functionally graded components. Functionally graded parts are parts in which the composition / microstructure of the component changes in different regions depending on the service environment encountered by that region. It is difficult to manufacture such components by conventional powder metallurgy methods, and long cycle times at high temperatures may even create undesirable phases. A HEEB-based system would allow the manufacture of truly functionally graded components, where the spatial distribution of material composition is controlled very accurately, and the formation of unwanted phases is entirely avoided. There are many other components other than turbine disks that could benefit from HEEB net shape casting, and this application area could very well be the one with the highest immediate payoff.

SUMMARY AND CONCLUSION

In this article, many of the possible benefits of HEEB-based materials processing were discussed as they apply to shock hardening, powder processing, and net-shape casting. Shock hardening can be implemented to a degree of precision not possible with conventional methods. Net shape casting will allow for the manufacture of unique near net shape functionally graded components. Welding was shown to be an application that will not necessarily benefit from HEEBs due to excessive heat flux, material damage from pulsed power parameters, difficult process control requirements, and radiation safety issues.

Currently, an intense experimental program is underway at Science Research Laboratory, Inc. and the MIT Materials Processing Center to realize the potential of many of these applications. Shock hardening is one of the planned experiments, and many others are being actively pursued together with concomitant advances in HEEB hardware and materials processing systems. Ceramic processing, powder metallurgy and powder processing, and heat treatment will all be pursued as the HEEB based approach is perfected, and the SNOMAD system will serve as a very versatile test platform in realizing the promise of HEEB materials processing.

ACKNOWLEDGMENTS

This work is being performed with support from the US Naval Surface Warfare Center and DARPA.

REFERENCES

1. N. C. Christofilos et al 1964. High Current Linear Induction Accelerator for Electrons. The Review of Scientific Instruments 35 (7) : 886 to 890.

2. D. L. Birx . Basic Principles Governing the Design of Magnetic Switches. LLNL UCID 18831.

3. D. L. Birx et al. Use of Induction Linacs with Nonlinear Magnetic Drive as High Average Power Accelerators. UCRL - 90878.

4. S.D. Putnam 1991. Fundamentals of Electron Beam Accelerators. Workshop on High Energy Electron Beam Welding ; Naval Surface Warfare Center.

5. D. S. Prono et al. 1989. High Average Power Induction LINACs. Proc. of the 1989 IEEE Particle Accelerator Conference. eds. F.B. Bennett and J. Kopta : 1441 - 1445.

6. I. Langmuir; K. Blodget 1924. Physical Review 24. page 49.

7. A. Septier 1967. The Focusing of Charged Particles, Vol. I & II: 27 New York : Academic Press.

8. W. B. Herrmannsfeldt 1988. EGUN - An Electron Optics and Gun Design Program. Stanford Linear Accelerator Center.

9. M. Lampe et al 1992. Fundamentals of High Energy Electron Beam Propagation. Proceedings of the AWS Conference on High Energy Electron Beam Welding and Materials Processing. American Welding Society.

10. A.C. Smith et al 1991. A Relativistic Electron Beam Approach to Atmospheric Welding and Surface Heat Treatment. JDR.

11. D. J. O'Keeffe, D. J. Pastine 1973. A Practical Guide to Accurate Grüneisen Equations of State. Metallurgical Effects at High Strain Rates : p. 157. New York : Plenum Press.

12. A. H. Cottrell 1953. Dislocations and Plastic Flow in Crystals. Oxford University Press.

13. G. I. Taylor 1934. The Mechanism of Plastic Deformation of Crystals. Proc. Royal Society of London. A 145. 362 to 387.

14. D. Kuhlmann-Wilsdorf 1962. A New Theory of Work Hardening. Trans. AIME 224. 1047 to 1061.

15. W. C. Leslie 1973. Microstructural Effects of High Strain Rate Deformation. Metallurgical Effects at High Strain Rates: p. 571. New York : Plenum Press.

16. L. F. Trueb 1970. Microstructural Study of Diamonds Synthesized under Conditions of High Temperature and Moderate Explosive Shock Pressure. Journal of Applied Physics 42 (2). 503 to 510.

17. D. G. Morris 1980. Compaction and Mechanical Properties of Metallic Glass. Metal Science June 1980. 215 to 220.

18. L. E. Murr et al 1983. Explosive Consolidation of an Amorphous Iron-Base Powder. Scripta Metallurgica 17. 1353 - 1357.

FIGURES

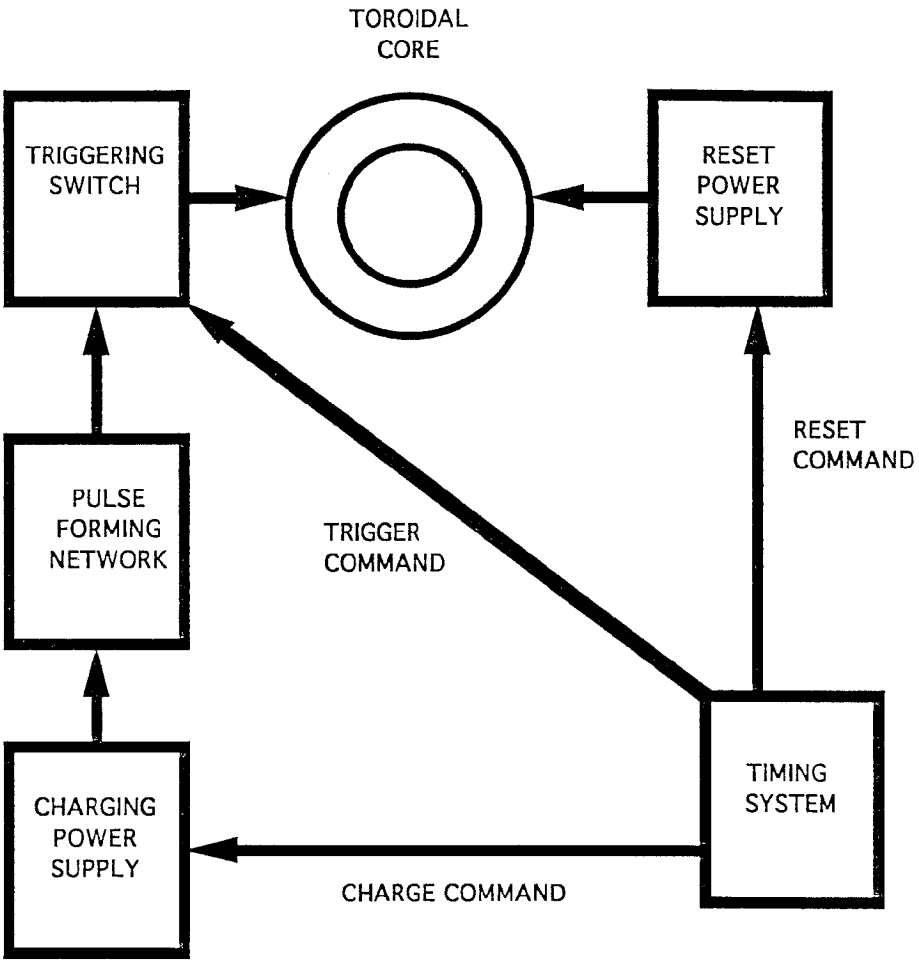

FIGURE 1

SCHEMATIC OF PULSE TRANSFORMER

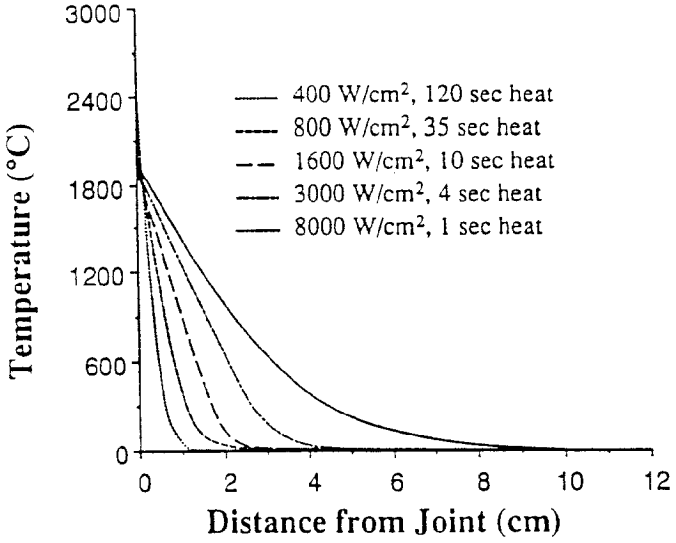

FIGURE 2

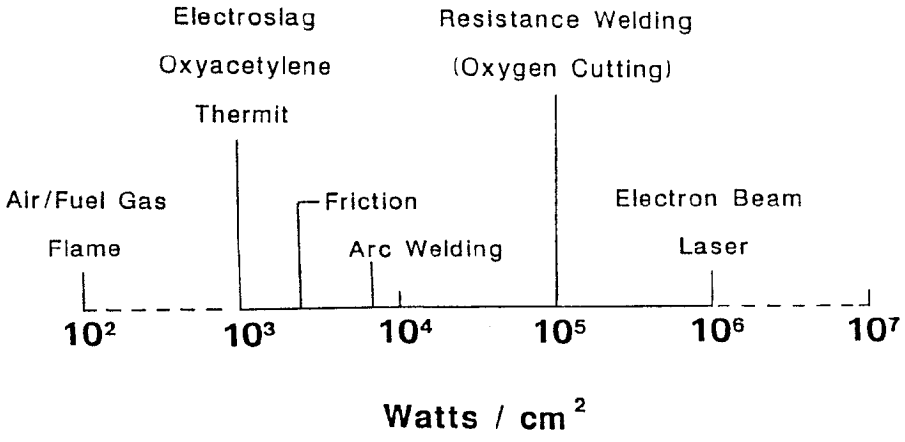

FIGURE 3

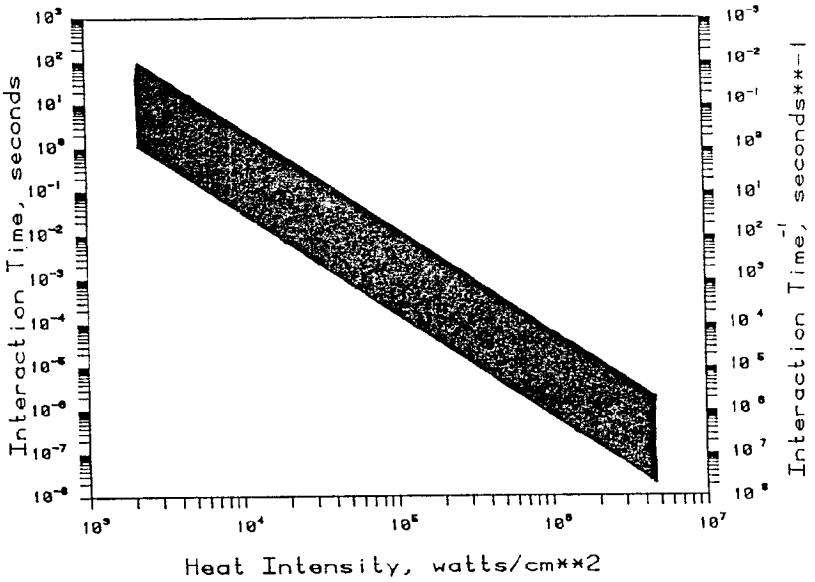

FIGURE 4

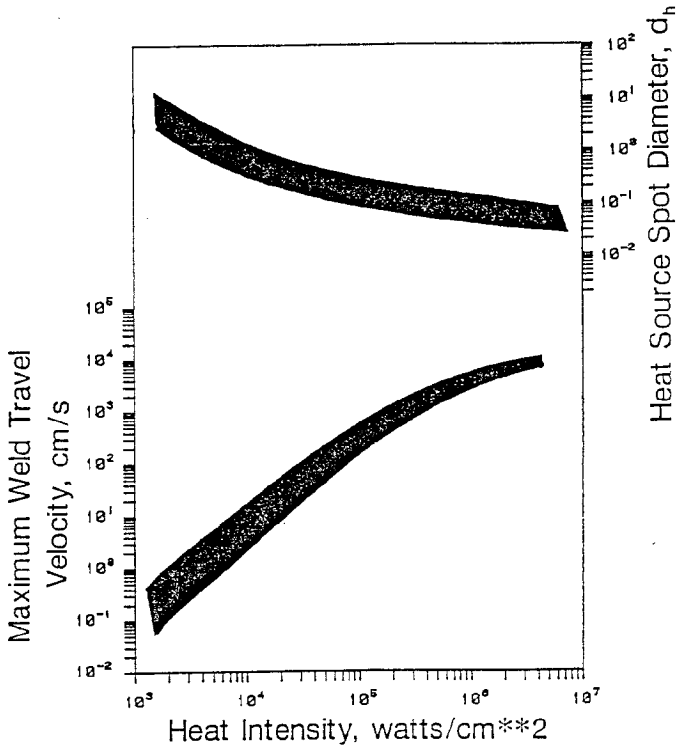

FIGURE 5

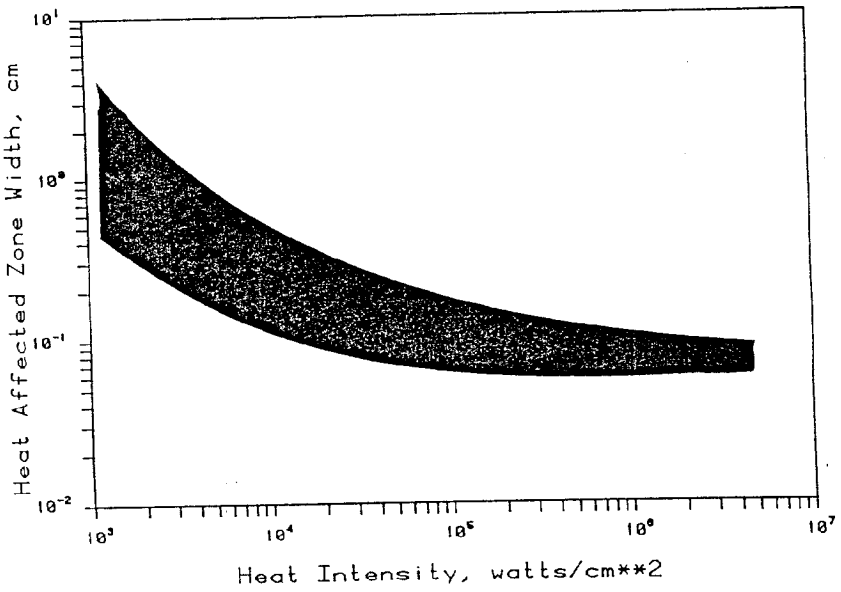

FIGURE 6

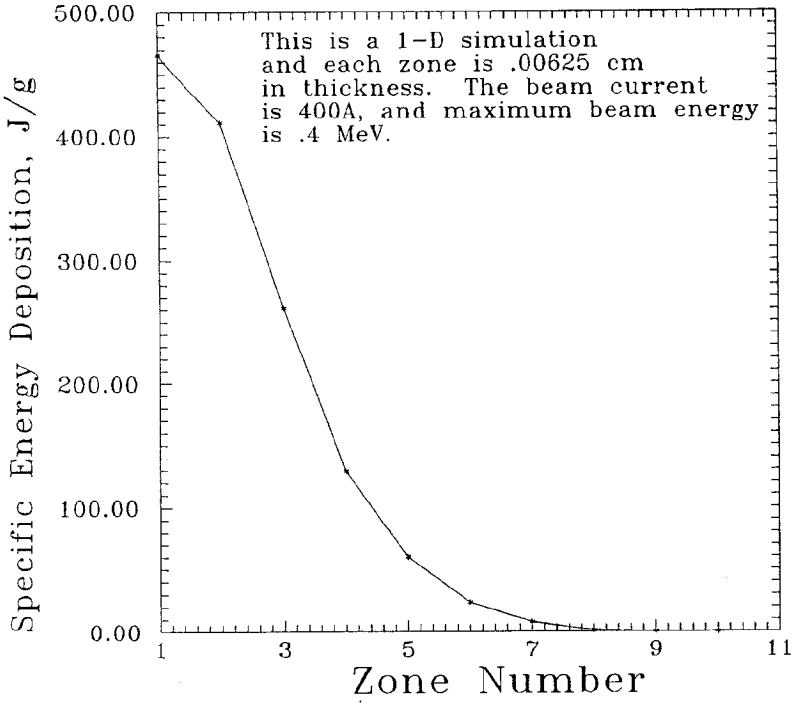

FIGURE 7

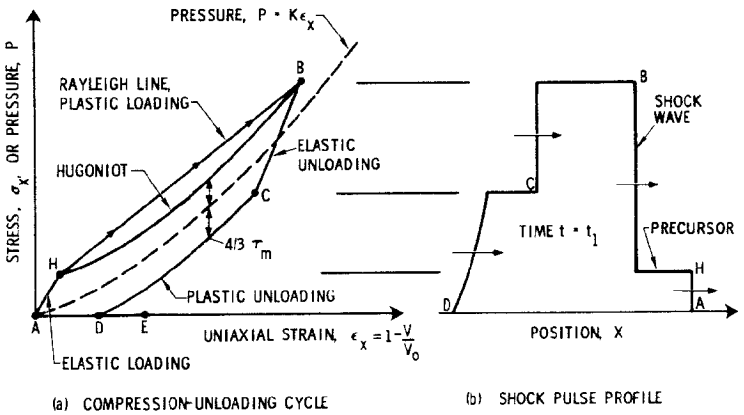

FIGURE 8

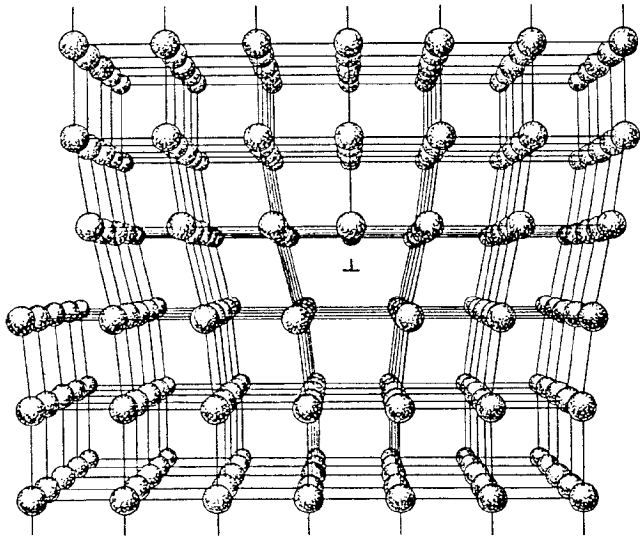

FIGURE 9

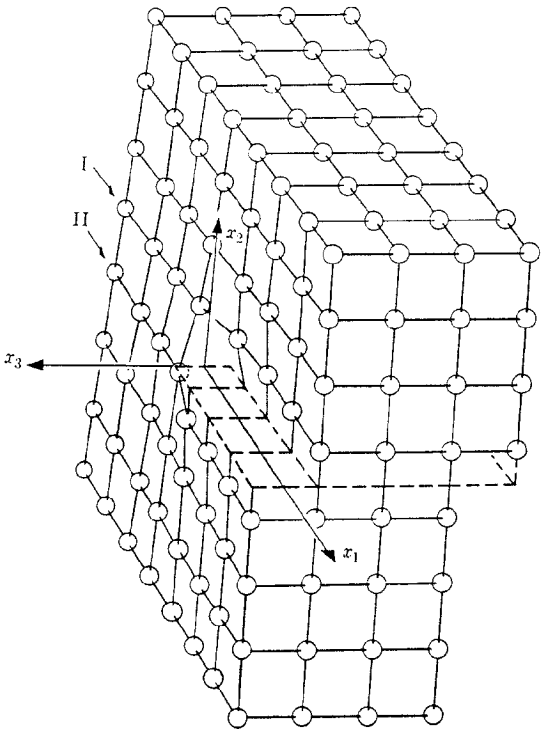

FIGURE 10

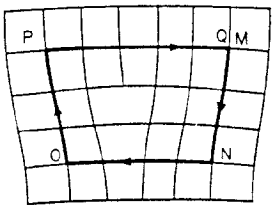

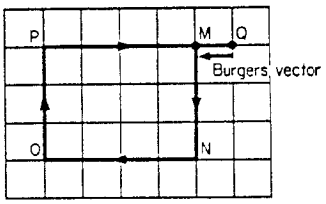

FIGURE 11

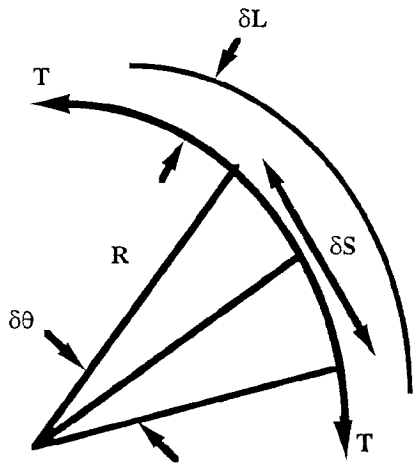

FIGURE 12

Assign a LINE TENSION - energy per unit length - to the dislocation segment

$$T = \alpha G b^2, \alpha < 1$$

We may derive the FORCE on the dislocation line by considering the work needed to move a segment δs through a distance δl . The shear displacement produced by this movement is given by the expression :

$$\left(\frac{\delta s \bullet \delta l}{A}\right) b$$

Where A is the slip plane area. The work is just the applied force times the displacement, so :

$$\delta W = A\tau \bullet \left(\frac{\delta s \cdot \delta l}{A}\right) b$$

so

$$\delta W = \tau b(\delta s \cdot \delta l) = \tau b \cdot \delta A$$

The FORCE PER UNIT LENGTH ON THE DISLOCATION LINE IS :

$$F = \frac{\delta W}{\delta A} = \tau b$$

Now by doing a force balance on the segment, force per unit length is balanced by the line tension :

$$T \cdot \delta\theta = \tau b \cdot \delta s$$

$$T = \alpha G b^2, \delta s = R \cdot \delta\theta$$

so

$$\tau = \frac{\alpha G b}{R}$$

This is the desired result : stress needed to bow dislocation segment

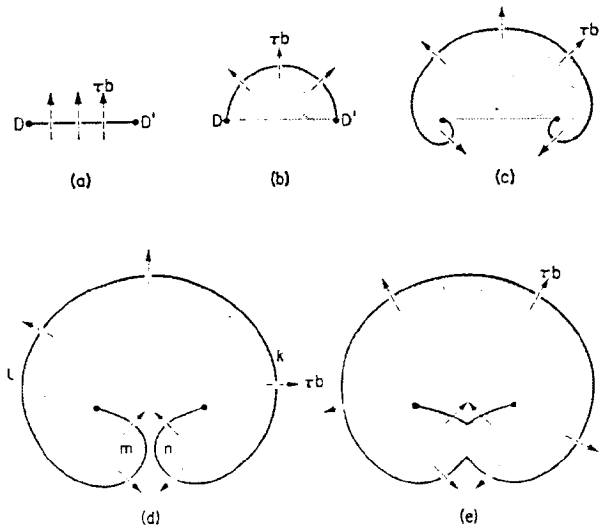

FIGURE 13

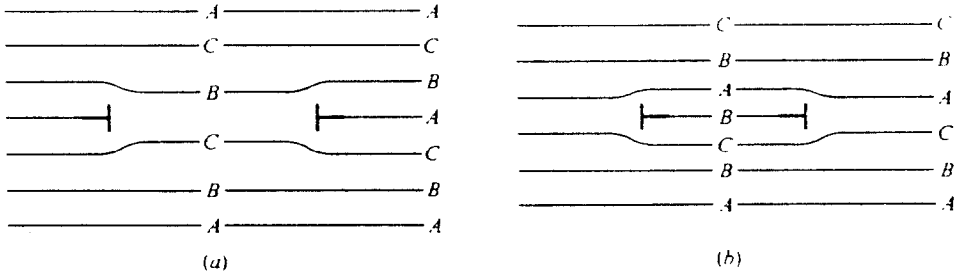

FIGURE 14

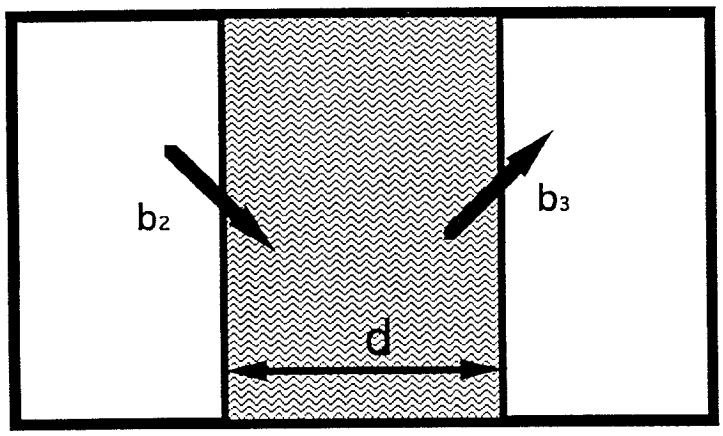

FIGURE 15

EXTENDED DISLOCATIONS

1. energetically, two partials may be favored over one larger dislocation :

$$\left\|\vec{b}_1\right\|^2 \geq \left\|\vec{b}_2\right\|^2 + \left\|\vec{b}_3\right\|^2$$

Where b_1 is the original dislocation, and b_2 and b_3 are the partials.

2. The partials will tend to repel.

3. The creation of a region of stacking fault takes energy γ_s per unit area

4. The repulsion force between the partials is given by:

$$F = \frac{G\left(\vec{b}_2 \bullet \vec{b}_3\right)}{2\pi d}$$

Where d is the spacing between them.

5. The equilibrium spacing occurs when F balances γ_s :

$$d = \frac{G\left(\vec{b}_2 \bullet \vec{b}_3\right)}{2\pi\gamma_s}$$

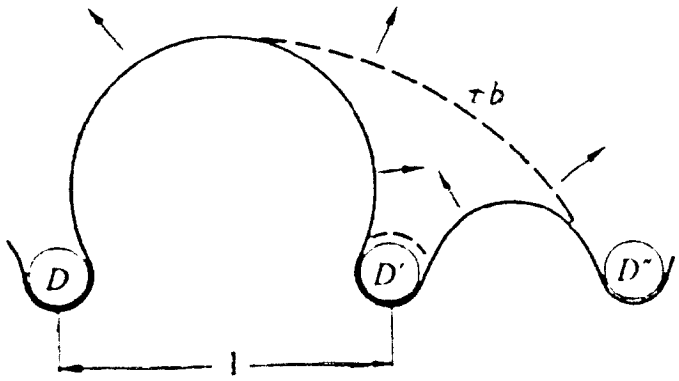

FIGURE 16

DISLOCATION INTERACTIONS WITH PRECIPITATES, INCLUSIONS, OR DISPERSED OXIDE PARTICLES

1. It was already shown that the stress needed to bow a dislocation segment to a radius R is given by :

$$\tau = \frac{\alpha G b}{R}$$

2. As the dislocation bends around the obstacles under the influence of the applied stress, it will eventually reach a radius of l / 2, at which point the configuration will be unstable, it will complete a loop around the obstacle, and will continue to move under the influence of the applied stress. The loop left behind around the obstacle will increase the effective diameter of the obstacle, and the next dislocation to pass this obstacle will see a " stronger" obstacle.

3. So the stress needed to overcome an array of obstacles with mean spacing l is :

$$\tau \approx \frac{\alpha G b}{l}$$

This quantity is known as the Orowan Stress.

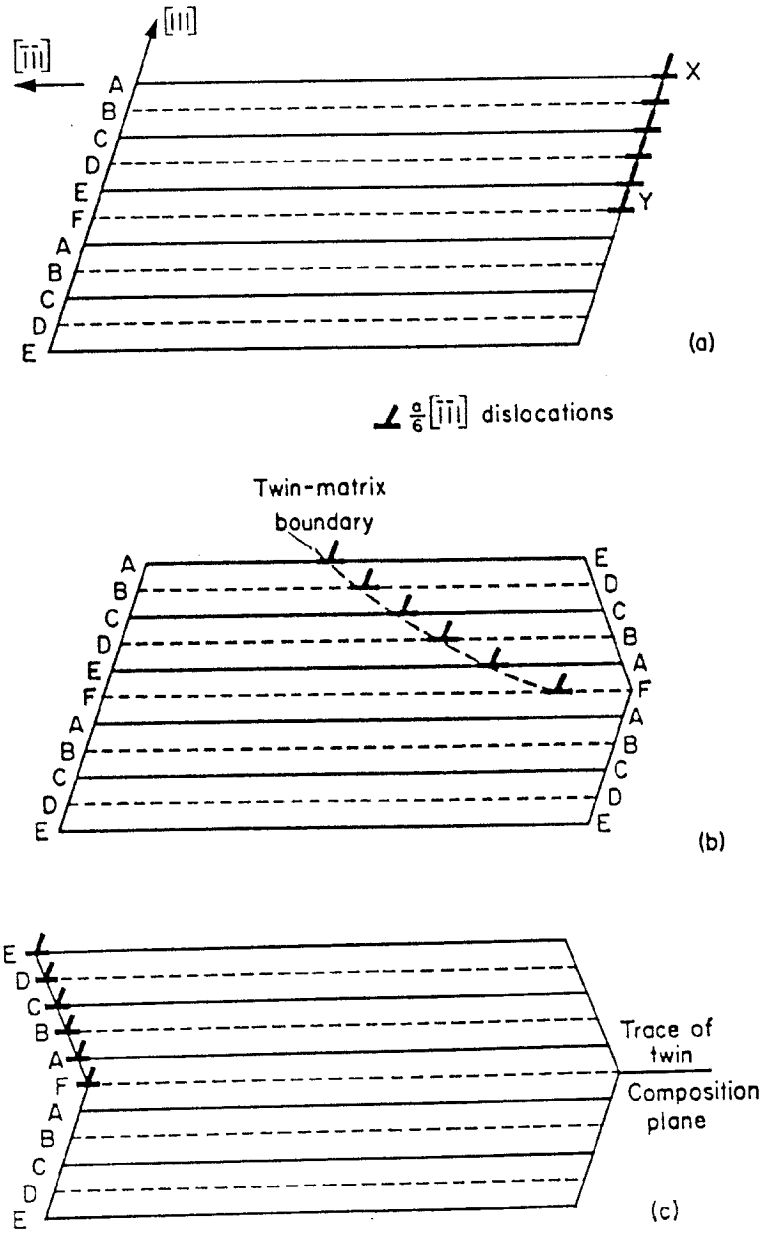
[111]
[1̄1̄1]
A
B
C
D
E
F
A
B
C
D
E
X
Y
(a)
a/6[1̄1̄1] dislocations
Twin-matrix boundary
A
B
C
D
E
F
A
B
C
D
E
E
D
C
B
A
F
A
B
C
D
E
(b)
E
D
C
B
A
F
A
B
C
D
E
Trace of twin
Composition plane
(c)

FIGURE 17

FIGURE CREDITS

1. Based on diagram in Ref. 1
2. T. W. Eagar
3. T. W. Eagar
4. T. W. Eagar
5. T. W. Eagar
6. T. W. Eagar
7. V. R. Dave
8. taken from : O. E. Jones 1973. Shock Wave Mechanics. Metallurgical Effects at High Strain Rates : p. 37. New York : Plenum Press.
9. taken from : F. A. McClintock; A. S. Argon 1966. Mechanical Behavior of Materials. Reading : Addison-Wesley Publishing Co.
10. taken from : F. A. McClintock; A. S. Argon 1966.
11. taken from : D. Hull 1965. Introduction to Dislocations. London : Pergamon Press.
12. V. R. Dave
13. taken from : P. Haasen 1986. Physical Metallurgy, 2nd ed. London : Cambridge University Press.
14. taken from : P. Haasen 1986.
15. V. R. Dave
16. taken from : P. Haasen 1986.
17. taken from : D. Hull 1965.